Progress In Electromagnetics Research, Vol. 143, 19–46, 2013

A REFINED TWO-DIMENSIONAL NONLINEAR CHIRP SCALING ALGORITHM FOR GEOSYNCHRONOUS EARTH ORBIT SAR

Tao Zeng, Wenfu Yang, Zegang Ding*, Dacheng Liu, and Teng Long

Radar Research Lab, Department of Electronic Engineering, Beijing Institute of Technology, Beijing 100081, P. R. China

Abstract—Taking into account long signal propagation time, curved orbit and "near-far-near" slant range histories at apogee, a refined slant range model (RSRM) is presented for geosynchronous earth orbit synthetic aperture radar (GEO SAR) in this paper. Additional linear component and high order components are introduced into straight orbit assumption (SOA) model to describe relative motion during long signal propagation and curved orbit respectively. And the special slant range histories at apogee are considered through adding terms changing with the sign of Doppler rate. Then, based on RSRM under an ideal acquisition and ignoring nonideal factors (such as depolarization and attenuation effects), a refined two-dimensional nonlinear chirp scaling algorithm (RTNCSA) is proposed. Space-variant range cell migration (RCM) caused by range-variant effective velocities is corrected by refined range nonlinear chirp scaling algorithm, and the variable Doppler parameters in azimuth direction are equalized through refined azimuth nonlinear chirp scaling algorithm. Finally, RSRM is verified by 600-second direct signal received by a stationary receiver on a tall building from BeiDou navigation satellite, and RTNCSA is validated through simulated point array targets with resolution of 5 m and scene size of 150 km.

1. INTRODUCTION

Geosynchronous earth orbit synthetic aperture radar (GEO SAR) is a satellite radar imaging mission in the geosynchronous earth orbit using a SAR. The concept of GEO SAR was proposed by Tomiyasu in

Received 12 July 2013, Accepted 16 September 2013, Scheduled 21 October 2013

* Corresponding author: Zegang Ding (z.ding@bit.edu.cn).

1978 [1, 2]. Due to its high temporal resolution and large coverage, GEO SAR can be well applied in a lot of areas such as geology structural mapping, flooding monitoring, sea ice monitoring and soil moisture mapping [3–7]. Recently, GEO SAR turns out to be a research hotspot. Jet Propulsion Laboratory (JPL) and Cranfield University devoted to the system design of GEO SAR and presented different projects respectively [8–11]. Compared with low earth orbit SAR (LEO SAR), GEO SAR has evident advantages, such as excellent temporal resolution and extremely large coverage [12]. However, with the increase of the satellite orbit altitude, the realization of GEO SAR faces great challenges such as huge power transmitter, big aperture antenna and complex imaging. This paper focuses on efficient frequency domain imaging algorithm of GEO SAR.

Recently, a lot of imaging algorithms for GEO SAR have been presented. A range migration algorithm (RMA) based on SOA model was presented in literature [13, 14], but this algorithm didn't take into account curved orbit and special slant range histories at apogee. Point array targets just with scene size of 2 km and resolution of 15 m can be focused by this algorithm, sub-scene algorithm should be adopted if processing larger scenes. Then based on the series expansion (SE) model, range-Doppler algorithm (RDA), chirp scaling algorithm (CSA) and nonlinear chirp scaling algorithm (NCSA) are presented in sequence [18–20]. The SE model is accurate, but the coefficient variances of SE model were neglected in RDA and CSA. Therefore, range cell migration (RCM) can't be corrected accurately by these two algorithms when the scene is large. NCSA can accomplish accurate range cell migration correction (RCMC) and focusing of large scene. In literature [20], point array targets with scene of 100 km and resolution of 12 m were focused well by NCSA. However, the azimuth-variant Doppler parameters were not taken into account in NCSA. Moreover, high resolution and the large scene would result in azimuth spectrum aliasing. Therefore the scene size and resolution are limited when using NCSA in literature [20]. In addition, Back projection algorithm (BPA) was utilized in GEO SAR as well [21]. Although BPA is very precise, it is time-consuming and hardly applied in practice. In order to process echo with high resolution and large scene, new imaging algorithm should be developed.

A refined two-dimensional nonlinear chirp scaling algorithm (RTNCSA) based on a refined slant range model (RSRM) is proposed in this paper. RSRM takes into account long signal propagation time, curved orbit and "near-far-near" slant range histories at apogee. RSRM is based on SOA model, and introduces additional linear component and high order components to describe the relative motion

during long signal propagation time and the curved orbit respectively. Moreover, the special slant range histories at apogee are considered via through adding terms changing with the sign of Doppler rate. Because the RCM and focusing parameters change in range and azimuth direction, RTNCSA is proposed to accomplish the processing GEO SAR echo with high resolution and large scene. First of all, two-step algorithm is adopted to unfold the azimuth spectrum. Then, refined range nonlinear chirp scaling algorithm (RRNCSA) is carried out to accomplish space-variant RCMC. Finally, the variant Doppler parameters in azimuth direction are equalized via refined azimuth nonlinear chirp scaling algorithm (RANCSA). RSRM is verified by 600-second direct signal received by a stationary antenna on the top of a tall building from the BeiDou navigation satellite. The direct signal is feasible for validating the slant range model. However, when developing imaging algorithm in practice, some problems in the two-way propagation path, such as depolarization and attenuation effects should be taken into account [22]. And RTNCSA is validated through simulated point array targets with resolution of 5 m and scene size of 150 km.

This paper is organized as follows. The signal model of GEO SAR is presented in Section 2. Section 3 introduces the 2-D frequency spectrum and RTNCSA. In Section 4, computer simulation and experimental results are performed to validate RSRM and RTNCSA. Section 5 draws the conclusion.

2. SIGNAL MODEL OF GEO SAR

The most remarkable advantage of GEO SAR is the excellent temporal resolution available from geosynchronous orbit. GEO SAR should operate on the inclined geosynchronous satellite orbit (IGSO) instead of the geostationary earth orbit because SAR requires relative satellite-Earth motion. The geometry of a typical GEO SAR is illustrated in Figure 1.

In Figure 1, H is the orbit altitude, R_e the average radius of the earth, v_s the satellite speed of GEO SAR in the earth-centred earth-fixed coordinate system, and v_b the beam velocity. The relation between v_s and v_b can be approximately expressed as

$$\frac{v_s}{v_b} \approx \frac{H + R_e}{R_e} \tag{1}$$

The satellite speed v_s is much bigger than v_b because the orbit altitude of GEO SAR is much larger than the average radius of the earth. The orbit elements of GEO SAR can be chosen as follow [23]:

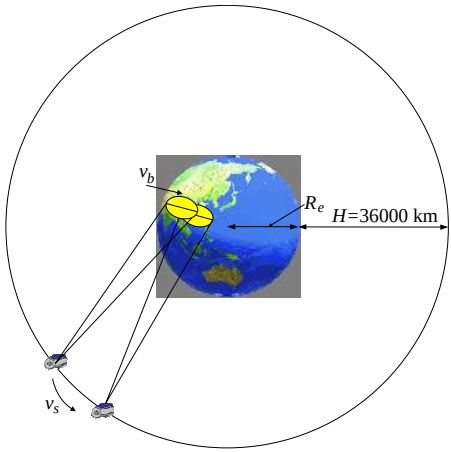

Figure 1. Geometry of GEO SAR.

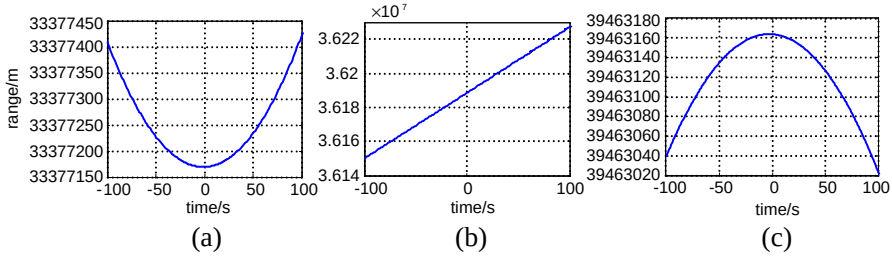

Figure 2. Slant range histories of GEO SAR in different position. (a) Perigee. (b) Equator. (c) Apogee.

semi-major axis is 42164.2 km, inclination is 53 degree, eccentricity is 0.07, argument of perigee is 270 degree, right ascension of ascending node is 110 degree and the down-looking angle is 4 degree. Considering S-band GEO SAR, the synthetic aperture time would be about two hundred seconds at perigee to approach resolution of 5 m. Besides, the characters of the echoes in GEO SAR at perigee, apogee and equator are almost completely different. Figure 2 and Figure 3 show the slant range histories and time-frequency graphs of GEO SAR respectively.

The slant range histories of target in the centre of the imaging scene at perigee, equator and apogee are shown in Figures 2(a)–(c) respectively. Obviously, slant range histories at perigee and equator are "far-near-far", but slant range histories at apogee are "near-far-near". If applying SOA model directly to model the slant range histories at apogee, the effective velocity will be an imaginary value. Therefore, new slant range model should be used in GEO SAR to represent the slant range histories at apogee.

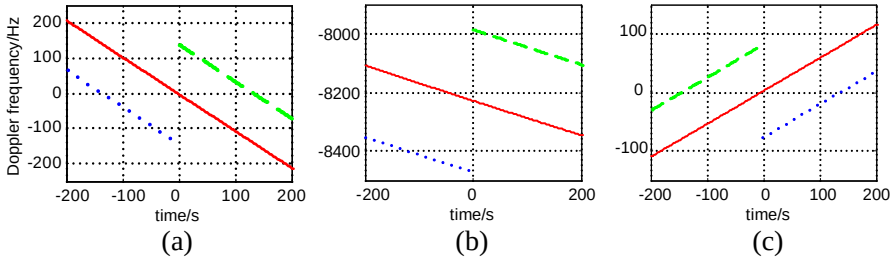

Figure 3. Time-frequency graphs of GEO SAR in different position. (a) Perigee. (b) Equator. (c) Apogee.

The time-frequency graphs of three targets in the scene at perigee, equator and apogee are illustrated in Figures 3(a)–(c) respectively. The red solid line denotes the time-frequency graph of the target in the scene centre, the green dashed line and blue dotted line stand for the targets at the edges of the scene. It is clear that the azimuth spectrum is aliasing because the whole Doppler bandwidth of the scene is larger than the typical PRF value of 200∼300 Hz. Therefore, the sub-aperture algorithm [24] or the two-step algorithm [25] should be adopted to avoid the azimuth spectrum aliasing.

Considering the features of GEO SAR mentioned above, a refined slant range model (RSRM) is presented in this paper and can be written as

$$\begin{aligned} R\left(t;r_0,x_0\right) = {} & \left[1+s_{fdr}\right]r_0 - s_{fdr}\sqrt{r_0^2+\left(v\left(r_0,x_0\right)t-x_0\right)^2} \\ & +\frac{v^2\left(r_0,x_0\right)}{c}\left(t-\frac{x_0}{v\left(r_0,x_0\right)}\right)+a\left(r_0,x_0\right)\left(t-\frac{x_0}{v\left(r_0,x_0\right)}\right)^3 \\ & +b\left(r_0,x_0\right)\left(t-\frac{x_0}{v\left(r_0,x_0\right)}\right)^4 \end{aligned} \tag{2}$$

where $R(t;\, r_0,\, x_0)$ is the target-to-satellite distance, $s_{fdr} = \mathrm{sign}(f_{dr})$, f_{dr} is the Doppler rate and sign$(\cdot)$ stands for signum function, t is the slow time, r_0 is the closest approach of the target, x_0 is the azimuth coordinate of target, $v(r_0, x_0)$ is effective velocity, c is the velocity of light, $a(r_0, x_0)$ and $b(r_0, x_0)$ are cubic and quartic order components of slant range respectively. And the expressions of $v(r_0, x_0)$, $a(r_0, x_0)$ and $b(r_0, x_0)$ are given in the Appendix A.

RSRM combines the benefits of the SOA model and the SE model. The linear component can be regarded as the effect of long signal propagation time. The additional cubic and quartic components are used for describing the curved orbit. Besides, the special slant range histories at apogee are taken into account by the terms with regard

to s_{fdr}. Although RSRM can satisfy the requirement of the slant range model for GEO SAR, the variances of the coefficients should be considered carefully when developing the imaging algorithm.

The variant coefficients of RSRM with respect to range position and azimuth position at perigee are given in Figure 4. Figure 4(a) shows the effective velocities of different targets. Range errors introduced by using a constant effective velocity are illustrated in Figure 4(b). Figure 4(c) and Figure 4(d) represent $a(r_0, x_0)$ and $b(r_0, x_0)$, respectively. According to Figure 4, range nonlinear chirp scaling is required to accomplish the range-variant RCMC caused by the space-variant effective velocities. Moreover, sub-scene algorithm [13] or azimuth nonlinear chirp scaling [27–29] should be adopted to avoid defocusing introduced by variant Doppler parameters in azimuth direction. The sub-scene algorithm is time-consuming; therefore, RTNCSA based on RSRM is proposed in next section.

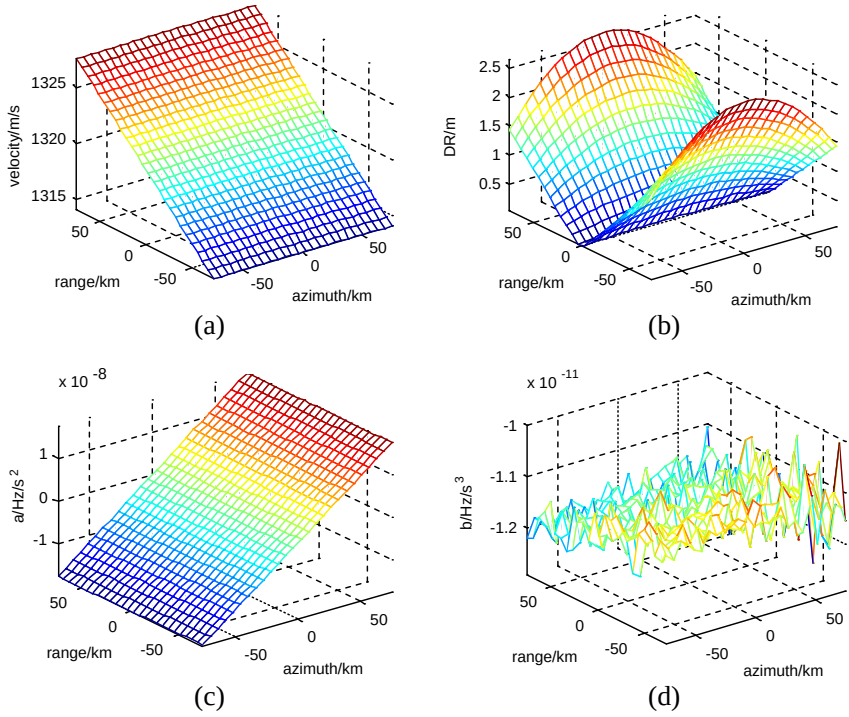

Figure 4. Variant coefficients of different targets in GEO SAR. (a) Effective velocities of different targets. (b) Range errors introduced by using a constant effective velocity. (c) Coefficient $a(r_0, x_0)$ of different targets. (d) Coefficient $b(r_0, x_0)$ of different targets.

3. REFINED TWO-DIMENSIONAL NONLINEAR CHIRP SCALING ALGORITHM

3.1. Description of Variant Coefficients

As discussed in Section 2, the coefficients of RSRM vary significantly both in range direction and azimuth direction. Range-variant RCMC and space-variant azimuth focusing are two challenges brought by the variable coefficients. Therefore, the variances of the coefficients should be modelled correctly.

The RCM is mainly affected by the variances of effective velocity in range direction. In order to implement accurate RCMC, the effective velocity is described by

$$v^2(r_0) \approx V_0 + V_1(r_0 - r_{ref}) + V_2(r_0 - r_{ref})^2 \tag{3}$$

where r_0 is the closest approach of the target, r_{ref} the reference slant range, and V_0, V_1, and V_2 are the coefficients decided by system parameters.

In addition, the quadratic and cubic components of Doppler parameters vary with azimuth time and can be expanded as Taylor series:

$$\begin{aligned} f_{dr} &= \frac{-2v^2(r_0, x_0)}{\lambda r_0} \approx f_{dr0}(r_0) + f_{dr1}(r_0)\, t_p + f_{dr2}(r_0)\, t_p^2 \\ a(r_0, x_0) &\approx a_{r0}(r_0) + a_{r1}(r_0)\, t_p \end{aligned} \tag{4}$$

where f_{dr} is the Doppler frequency rate, t_p the time when the slant range of target approaching closest slant range, and λ the wavelength. $f_{dr0}(r_0)$, $f_{dr1}(r_0)$, $f_{dr2}(r_0)$, $a_{r0}(r_0)$, and $a_{r1}(r_0)$ are the Taylor series coefficients of f_{dr} and $a(r_0, x_0)$ respectively, and they are obtained by analytical method.

3.2. Block Diagram of RTNCSA

In order to solve aforementioned two problems, RTNCSA is presented in this paper and the block diagram of RTNCSA is shown in Figure 5. First of all, azimuth filtering is accomplished to avoid azimuth spectrum aliasing. As illustrated in Figure 5(a) and Figure 5(b), three lines stand for time-frequency graphs of three targets in one azimuth line, and the whole Doppler frequency bandwidth B_a of the raw data is larger than PRF. After the azimuth filtering, Doppler frequency bandwidth B_s is smaller than PRF and the azimuth spectrum aliasing is removed. However, the slopes of the three lines are different because the Doppler parameters of targets in one azimuth line are variable.

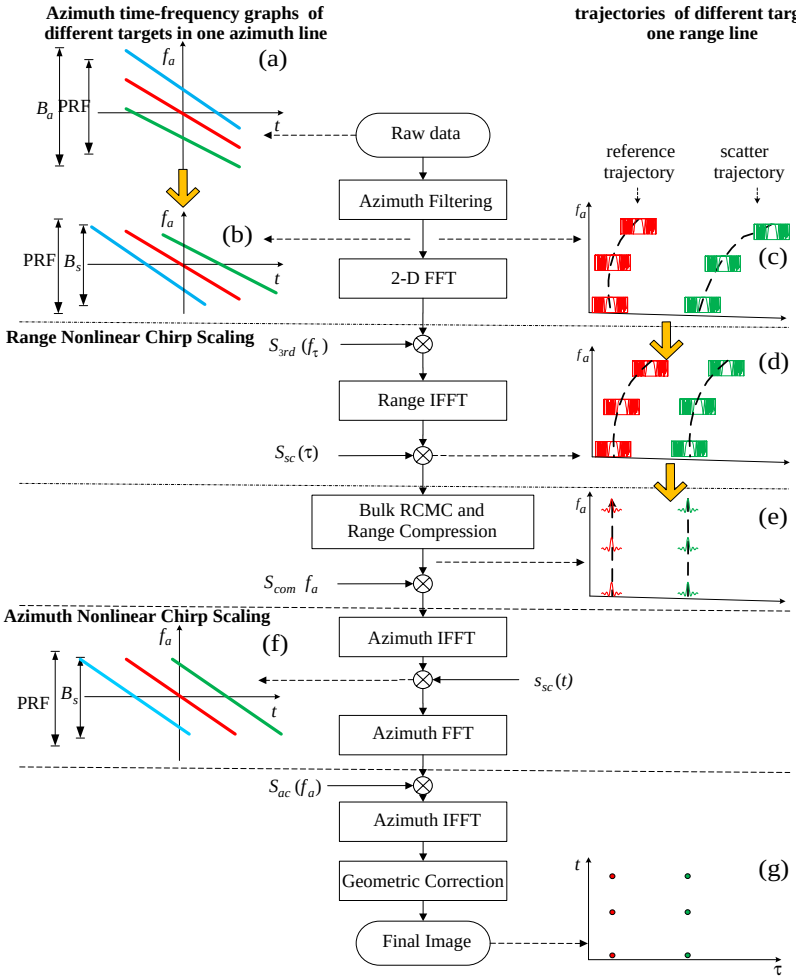

Figure 5. Block diagram of RTNCSA. (a), (b) and (f) are the azimuth time-frequency graphs of three different targets in one azimuth line, (c), (d) and (e) are the trajectories in range-Doppler domain of targets in one range line, and (g) is the final image.

2-D FFT takes the raw data to 2-D frequency domain then. The processes of range focusing are illuminated in Figure 5(c), Figure 5(d) and Figure 5(e). In order to complete the range-variant RCMC, range nonlinear chirp scaling is fulfilled through a cubic filtering, range inverse FFT and nonlinear chirp scaling function multiplication. Then bulk RCMC and range compression are done via multiplying each range line by a phase function in the 2-D frequency domain.

After the range compression, a range inverse FFT takes the data to range-Doppler domain, where each azimuth line is multiplied by an azimuth compensation phase function. Then as given in Figure 5(f), the azimuth Doppler parameters equalization is performed by an azimuth FFT and azimuth nonlinear chirp scaling phase function multiplication, and the slopes of the three lines turn out to be equal. Finally, the azimuth compression filter multiplication, an azimuth inverse FFT and geometric correction are implemented to achieve the final image as shown in Figure 5(g).

3.3. Azimuth Spectrum Unfolding and 2-D Spectrum

The azimuth spectrum of GEO SAR is aliasing according to the analysis in Section 2. Before 2-D focusing, the azimuth spectrum should be unfolded. Based on the RSRM proposed in Section 2, the echo of GEO SAR is given by

$$\begin{aligned} s_r(\tau, t; r_0, x_0) = w_r\left(\tau - \frac{2R(t; r_0, x_0)}{c}\right) w_a(t) \\ \exp\left(j\pi k_r\left(\tau - \frac{2R(t; r_0, x_0)}{c}\right)^2\right) \\ \exp\left(-j4\pi\frac{R(t; r_0, x_0)}{\lambda}\right) \end{aligned} \tag{5}$$

where $s_r(\tau, t; r_0, x_0)$ is the echo, τ is the fast time, t is the slow time, $R(t; r_0, x_0)$ is the slant range between radar and the target, c is the speed of the light, $w_r(\cdot)$ and $w_a(\cdot)$ are the envelops of the range signal and azimuth signal, k_r is the chirp rate of the transmitted signal, and λ is the wavelength.

This paper adopts two-step algorithm [25] to avoid azimuth spectrum aliasing and the process can be given by

$$\begin{aligned} s_r(\tau, t; r_0, x_0) = \underbrace{\exp\left(\frac{-j2\pi v^2(r_{ref})t^2}{\lambda r_{ref}}\right)}_{\text{Compensation Phase}} \int s_r(\tau, z; r_0, x_0) \\ \cdot \underbrace{\exp\left(\frac{j2\pi v^2(r_{ref})z^2}{\lambda r_{ref}}\right)}_{dechirp} \cdot \underbrace{\exp\left(-j2\pi\frac{2v^2(r_{ref})tz}{\lambda r_{ref}}\right)}_{FFT} dz \end{aligned} \tag{6}$$

where $s_r(\tau, z; r_0, x_0)$ is the raw signal, and $s(\tau, t; r_0, x_0)$ is the signal after azimuth spectrum unfolding.

The precise 2-D frequency spectrum is the foundation of imaging algorithm, and can be obtained through applying principle of stationary phase (POSP) in range and azimuth direction. The 2-D spectrum is given by

$$S\left(f_\tau, f_a; r_0, x_0\right) = W_r\left(\frac{f_\tau}{k_r}\right) W_a\left(\frac{s_{fdr} c r_0 f_a}{2v^2\left(r_0, x_0\right)\left(f_c + f_\tau\right)\sqrt{1 - \frac{c^2 f_a^2}{4v^2(r_0,x_0)(f_c+f_\tau)^2}}}\right) \cdot \exp\left\{ j \left[\begin{array}{l} -\dfrac{\pi f_\tau^2}{k_r} - \dfrac{4\pi\left[1 + s_{fdr}\right] r_0\left(f_\tau + f_c\right)}{c} \\ +4\pi s_{fdr} r_0 \sqrt{\left(\dfrac{f_\tau + f_c}{c}\right)^2 - \left[\dfrac{f_a}{2v\left(r_0, x_0\right)}\right]^2} \\ -\dfrac{4\pi\left(f_\tau + f_c\right)}{c}\left[a\left(r_0, x_0\right)\left(t^*\right)^3 + b\left(r_0, x_0\right)\left(t^*\right)^4\right] \end{array} \right] \right\} \quad (7)$$

where $S(f_\tau, f_a; r_0, x_0)$ is the 2-D spectrum, f_τ and f_a are range frequency and Doppler frequency respectively, $W_r(\cdot)$ and $W_a(\cdot)$ are the envelopes of range spectrum and azimuth spectrum respectively, f_c is the carrier frequency, t^* is the azimuth stationary point and can be written as

$$t^* = s_{fdr} \frac{c r_0 f_a}{2\left(f_c + f_\tau\right) v^2\left(r_0, x_0\right)\sqrt{1 - \left(\frac{c f_a}{2v(r_0,x_0)(f_c+f_\tau)}\right)^2}}. \quad (8)$$

When obtaining the azimuth stationary point, the terms concerning $a(r_0, x_0)$ and $b(r_0, x_0)$ in RSRM are ignored because they are very small. It is the only approximation and the accuracy of the spectrum is proved in Section 4. Compared with classical spectrum, just a constant phase term and two high order components are added to the new 2-D spectrum.

3.4. Refined Range Nonlinear Chirp Scaling

After azimuth spectrum unfolding, RCMC and 2-D focusing should be implemented to achieve the final image. According to analysis in Section 2, the variance of effective velocity can't be ignored. In this paper, RRNCSA based on RSRM is adopted to accomplish the accurate RCMC.

First of all, the signal of GEO SAR after azimuth spectrum unfolding is transformed to 2-D spectrum as given by Equation (7), and its phase can be expressed as a series of f_τ:

$$\Phi(f_\tau, f_a; r_0, x_0) = \underbrace{\frac{4\pi s_{fdr} r_0 f_c \gamma\left(r_0, f_a\right)}{c}}_{\text{range modulation term}} \underbrace{- \frac{4\pi\left(1 + s_{fdr}\right) r_0 f_c}{c}}_{\text{constant phase}}$$

$$+\underbrace{2\pi\left(\frac{2s_{fdr}r_0}{c\gamma\left(r_0,f_a\right)}-\frac{2\left(1+s_{fdr}\right)r_0}{c}\right)f_\tau}_{\text{range cell migration term}}$$

$$+\underbrace{\left(-\frac{\pi}{k_r}-\frac{\pi s_{fdr}r_0cf_a^2}{2f_c^3v^2\gamma^3\left(r_0,f_a\right)}\right)f_\tau^2}_{\text{range modulation term}}+\underbrace{\frac{\pi s_{fdr}r_0cf_a^2}{2f_c^4v^2\gamma^5\left(r_0,f_a\right)}f_\tau^3}_{\text{coupling term}} \tag{9}$$

where $\gamma(f_a;r_0)=\sqrt{1-(\frac{cf_a}{2f_cv(r_0)})^2}$.

According to Equation (9), the expression is similar to that of literature [26], it is easy to update algorithm from classical NCSA. However, all the coefficients of presented algorithm are different from that of classical NCSA. Therefore, we propose the steps of new algorithm as following.

In the 2-D frequency domain, the signal is multiplied by a cubic phase term which is given by

$$S_{3rd}=\exp\left[j\frac{2\pi}{3}\left(Y_m\left(f_a\right)-\frac{3}{4\pi}\frac{\pi s_{fdr}r_0cf_a^2}{f_c^4v^2\gamma^5\left(r_0,f_a\right)}\right)f_\tau^3\right]. \tag{10}$$

Then, range inverse Fourier transformation takes the signal to the range-Doppler domain:

$$s\left(\tau,f_a\right)=\exp\left[-j\pi K_m\left(\tau-\tau_d\right)^2-j\frac{2\pi}{3}Y_mK_m^3\left(\tau-\tau_d\right)^3\right]. \tag{11}$$

where τ_d is short for target trajectory $\tau_d(r_0,\ f_a)$, K_m is short for the range-frequency rate $K_m(r_0;\ f_a)$, and they can be written as

$$\tau_d\left(r_0,f_a\right)=\frac{2\left(1+s_{fdr}\right)r_0}{c}-\frac{2s_{fdr}r_0}{c\gamma\left(r_0,f_a\right)}. \tag{12}$$

$$K_m\left(f_a;r_0\right)=\frac{1}{-\frac{1}{k_r}-\frac{s_{fdr}r_0cf_a^2}{2f_c^3v^2\gamma^3(r_0,f_a)}}\approx K_{mref}+K_s\ \Delta\tau\left(f_a;r_0\right). \tag{13}$$

where K_s is the slope of range-frequency rate and $(f_a;r_0)$ is the difference between delay time from r_0 and that from reference range.

The chirp scaling phase function is given by

$$S_{sc}=\exp\left[-j\pi q_2\left(\tau-\tau_d\left(r_{ref},f_a\right)\right)^2-j\frac{2\pi}{3}q_3\left(\tau-\tau_d\left(r_{ref},f_a\right)\right)^3\right]. \tag{14}$$

The coefficients in the cubic filter and chirp scaling phase function are represented by

$$\begin{cases}q_2=K_{mref}\left(\alpha_v-1\right)\\ q_3=\frac{K_s(\alpha_v-1)}{2}-\alpha_v^2K_{mref}\beta_v\\ Y_m=\frac{K_s(\alpha_v-0.5)-\alpha_v^2K_{mref}\beta_v}{K_{mref}^3(\alpha_v-1)}\end{cases}. \tag{15}$$

where K_{mref}, α_v, β_v, K_s and Y_m are short for $K_m(r_{ref};\, f_a)$, $\alpha_v(f_a)$, $\beta_v(f_a)$, $K_s(f_a)$, $Y_m(f_a)$ respectively, and the expressions of α_v, β_v and K_s are given in Appendix B.

After range chirp scaling, the accurate RCMC and range focusing can be implemented by a conjugate multiplication in the 2-D frequency domain, and the phase of the range focusing filter is given by

$$\phi_{rc-mf}\left(f_\tau, f_a\right) = 2\pi\left[\tau_{ref}\left(f_a\right) - \tau_{ref}\left(f_{aref}\right)\right] f_\tau + \frac{\pi f_\tau^2}{\alpha_v K_{mref}} + \frac{2\pi\left(q_3 + Y_m K_{mref}^3\right) f_\tau^3}{3\alpha_v^3 K_{mref}^3}. \tag{16}$$

where f_{aref} is the reference Doppler frequency.

After the signal is transformed to range-Doppler domain, the phase correction function can be written as

$$\phi\left(f_a; r_0\right) = -\pi K_{mref}\left(1 - \frac{1}{\alpha_v}\right)\tau^2\left(r_0; f_a\right) - \left[\frac{\pi K_s}{3}\left(1 - \frac{1}{\alpha_v}\right) - \frac{2\pi K_{mref}}{3}\beta\left(2 - \alpha_v\right)\right]\tau^3\left(r_0; f_a\right). \tag{17}$$

where $\phi(f_a; r_0)$ is the correction phase.

3.5. Refined Azimuth Nonlinear Chirp Scaling

3.5.1. Derivation of Refined Azimuth Nonlinear Chirp Scaling

After RCMC, range compression and azimuth phase correction, the phase of signal in range-Doppler domain can be expressed as

$$\Phi\left(f_a; r_0, x_0\right) = \frac{4 s_{fdr}\pi r_0}{\lambda}\sqrt{1 - \left(\frac{\lambda f_a}{2v\left(r_0, x_0\right)}\right)^2} - \frac{4\pi}{\lambda}\left[a\left(r_0, x_0\right)\left(t^*\right)^3 + b\left(r_0\right)\left(t^*\right)^4\right] \tag{18}$$

The quartic order Taylor series of Equation (18) about f_a is given by

$$\Phi\left(f_a; r_0, x_0\right) = \frac{\pi s_{fdr} f_a^2}{f_{dr}} + \frac{4\pi s_{fdr} a_{r0} f_a^3}{\lambda f_{dr0}^3} + \pi a_{rt} t_p f_a^3 - \frac{4\pi b\left(r_0\right) f_a^4}{\lambda f_{dr0}^4} - \frac{\pi s_{fdr} r_0 \lambda^3 f_a^4}{32 v^4} + O\left(f_a^5\right) \tag{19}$$

where

$$a_{rt} = \frac{4 s_{fdr}}{\lambda}\left(-3\frac{a_{r0} f_{dr1}}{f_{dr0}^4} + \frac{a_{r1}}{f_{dr0}^3}\right). \tag{20}$$

As indicated in Equation (19), the Doppler parameters vary both in range direction and azimuth direction. Range-dependent Doppler parameters can be handled through variant filters in different range gates. RANCSA is proposed in this paper to equalize the azimuth-dependent Doppler parameters [27–29].

First of all, range-Doppler signal is multiplied by a phase compensation function:

$$S_{com}(f_a; r_0) = \exp\left\{ j\pi p_3 f_a^3 + j\pi p_4 f_a^4 - j\frac{4\pi s_{fdr} a_{r0}(r_0) f_a^3}{\lambda f_{dr0}^3} + j\frac{4\pi b(r_0) f_a^4}{\lambda f_{dr0}^4} + j\frac{\pi s_{fdr} r_0 \lambda^3 f_a^4}{32 v^4(r_0)} \right\} \quad (21)$$

where p_3 and p_4 are the cubic and quartic coefficients of the compensation phase respectively. The last three terms are employed to remove the constant high order phase terms, and the first two terms are introduced to avoid azimuth distortion caused by RANCSA. The signal after compensation can be given by

$$S_{acom}(f_a; r_0, x_0) = \exp\left\{ j\frac{\pi s_{fdr} f_a^2}{f_{dr}} + j\pi a_{rt} t_p f_a^3 + j\pi p_3 f_a^3 + j\pi p_4 f_a^4 \right\} \quad (22)$$

After phase compensation, applying POSP in the azimuth inverse Fourier transformation, 2-D time domain signal is given by

$$\varphi(t, t_p; r_0) = -\pi s_{fdr} f_{dr} (t - t_p)^2 - \pi (p_3 + a_{rt} t_p) s_{fdr} f_{dr}^3 (t - t_p)^3 + \pi p_4 f_{dr}^4 (t - t_p)^4 \quad (23)$$

It should be noted that an approximation is made to the azimuth stationary point, assuming that the third and higher order phase terms are small enough and can be ignored [26]. Then the RANCSA is performed through multiplying the 2-D time domain signal by the following phase function:

$$s_{sc}(t) = \exp\left\{ j\pi \left(q_2 t^2 + q_3 t^3 + q_4 t^4 \right) \right\}. \quad (24)$$

After phase function multiplication, azimuth Fourier transformation is performed to take the signal to range-Doppler domain again. And the phase of scaled signal is given by

$$\begin{aligned} \Phi_{sc}(f_a; r_0, x_0) = & -2\frac{\pi (f_a - s_{fdr} f_{dr} t_p) f_a}{q_2 - s_{fdr} f_{dr}} + \frac{\pi}{(q_2 - s_{fdr} f_{dr})^2} \\ & \left[(q_2 (f_a - s_{fdr} f_{dr} t_p))^2 - s_{fdr} (f_{dr} (f_a - q_2 t_p))^2 \right] \\ & + \frac{\pi}{(q_2 - s_{fdr} f_{dr})^3} \left[(q_3 (f_a - s_{fdr} f_{dr} t_p))^3 \right. \\ & \left. - (p_3 + a_{rt} t_p) s_{fdr} f_{dr}^3 (f_a - t_p q_2)^3 \right] \end{aligned}$$

$$+\frac{\pi}{(q_2-s_{fdr}f_{dr})^4}\left[(q_4(f_a-s_{fdr}f_{dr}t_p))^4+p_4f_{dr}^4(f_a-t_pq_2)^4\right] \tag{25}$$

where

$$\begin{cases}\dfrac{1}{(q_2-s_{fdr}f_{dr})^2}=\dfrac{1}{(q_2-s_{fdr}f_{dr0})^2}+\dfrac{2s_{fdr}(f_{dr1}t_p+f_{dr2}t_p^2)}{(q_2-s_{fdr}f_{dr0})^3}\\ \dfrac{1}{(q_2-s_{fdr}f_{dr})^3}=\dfrac{1}{(q_2-s_{fdr}f_{dr0})^3}+\dfrac{3s_{fdr}(f_{dr1}t_p+f_{dr2}t_p^2)}{(q_2-s_{fdr}f_{dr0})^4}\\ \dfrac{1}{(q_2-s_{fdr}f_{dr})^4}=\dfrac{1}{(q_2-s_{fdr}f_{dr0})^4}+\dfrac{4s_{fdr}(f_{dr1}t_p+f_{dr2}t_p^2)}{(q_2-s_{fdr}f_{dr0})^5}\end{cases} \tag{26}$$

$\Phi_{sc}(f_a;r_0,x_0)$ can be expressed as series of t_p and f_a:

$$\begin{aligned}\Phi_{sc}(f_a;r_0,x_0)\approx\ & F_1(q_2,q_3,q_4,p_3,p_4,f_a,f_a^2,f_a^3,f_a^4)+F_2(q_2,q_3,q_4,p_3,p_4)\,t_pf_a\\ &+F_3(q_2,q_3,q_4,p_3,p_4)\,t_p^2f_a+F_4(q_2,q_3,q_4,p_3,p_4)\,t_pf_a^2\\ &+F_5(q_2,q_3,q_4,p_3,p_4)\,t_p^2f_a^2+F_6(q_2,q_3,q_4,p_3,p_4)\,t_pf_a^3\\ &+F_7(q_2,q_3,q_4,p_3,p_4,t_p,t_p^2,t_p^3,t_p^4)\end{aligned} \tag{27}$$

where the coefficients can be expressed as

$$\begin{cases}F_1(q_2,q_3,q_4,p_3,p_4,f_a,f_a^2,f_a^3,f_a^4)=\dfrac{\pi}{-q_2+s_{fdr}f_{dr0}}f_a^2+\dfrac{\pi(-q_3+s_{fdr}p_3f_{dr0}^3)}{(-q_2+s_{fdr}f_{dr0})^3}f_a^3\\ \qquad\qquad+\dfrac{\pi(q_4+p_4f_{dr0}^4)}{(-q_2+s_{fdr}f_{dr0})^4}f_a^4\\ F_2(q_2,q_3,q_4,p_3,p_4)=\dfrac{2s_{fdr}\pi f_{dr0}}{q_2-s_{fdr}f_{dr0}}\\ F_3(q_2,q_3,q_4,p_3,p_4)=\pi\dfrac{3f_{dr0}^2(q_3-s_{fdr}q_2^2p_3f_{dr0})+2s_{fdr}f_{dr1}q_2(q_2-s_{fdr}f_{dr0})}{(q_2-s_{fdr}f_{dr0})^3}\\ F_4(q_2,q_3,q_4,p_3,p_4)=s_{fdr}\pi\dfrac{3f_{dr0}(-q_3+q_2p_3f_{dr0}^2)-f_{dr1}(q_2-s_{fdr}f_{dr0})}{(q_2-s_{fdr}f_{dr0})^3}\\ F_5(q_2,q_3,q_4,p_3,p_4)=\dfrac{\pi}{(-q_2+s_{fdr}f_{dr0})^4}\begin{bmatrix}-s_{fdr}f_{dr2}q_2^2+2f_{dr2}q_2f_{dr0}\\ -s_{fdr}f_{dr2}f_{dr0}^2-f_{dr1}^2q_2+s_{fdr}f_{dr1}^2f_{dr0}\\ -6f_{dr1}f_{dr0}q_3-3s_{fdr}f_{dr1}q_3q_2\\ +9s_{fdr}f_{dr1}q_2^2p_3f_{dr0}^2+3f_{dr0}^3s_{fdr}q_2^2a_{rt}\\ -3f_{dr0}^4q_2a_{rt}+6f_{dr0}^2q_4+6f_{dr0}^4p_4q_2^2\end{bmatrix}\\ F_6(q_2,q_3,q_4,p_3,p_4)=\pi\dfrac{\begin{array}{c}f_{dr0}\left[a_{rt}f_{dr0}^2(-s_{fdr}q_2+f_{dr0})-4s_{fdr}q_4-4f_{dr0}^3q_2p_4\right]\\ -3s_{fdr}f_{dr1}(-q_3+q_2p_3f_{dr0}^2)\end{array}}{(-q_2+s_{fdr}f_{dr0})^4}\end{cases}. \tag{28}$$

In order to equalize the variable Doppler parameters in azimuth direction and eliminate the azimuth distortion, the coefficients in Equation (27) should satisfy following equations:

$$\begin{cases}F_2(q_2,q_3,q_4,p_3,p_4)=-\dfrac{\pi}{\alpha_a}\\ F_3(q_2,q_3,q_4,p_3,p_4)=0\\ F_4(q_2,q_3,q_4,p_3,p_4)=0\\ F_5(q_2,q_3,q_4,p_3,p_4)=0\\ F_6(q_2,q_3,q_4,p_3,p_4)=0\end{cases} \tag{29}$$

where α_a is a constant scaling factor, and Equation (29) can be solved to give

$$\begin{cases} q_2 = -s_{fdr}\left(2\,\alpha_a - 1\right) f_{dr0} \\ q_3 = -\frac{1}{3} s_{fdr}\left(2\alpha_a - 1\right) f_{dr1} \\ q_4 = \frac{4\alpha_a f_{dr0} f_{dr2} + f_{dr1}^2 (5-14\alpha_a) + 3a_{rt} f_{dr0}^4 (1-2\alpha_a)}{12 s_{fdr} f_{dr0}} \\ p_3 = \frac{1}{3} \frac{f_{dr1}(4\alpha_a - 1)}{f_{dr0}^3 (2\alpha_a - 1)} \\ p_4 = \frac{\left(3a_{rt} f_{dr0}^4 + 5 f_{dr1}^2\right)(1-4\alpha_a) + 4 f_{dr2} f_{dr0} \alpha_a}{12 s_{fdr} f_{dr0}^5 (2\alpha_a - 1)} \end{cases} \tag{30}$$

Combining Equations (26)∼(30) with Equation (25), the signal after RANCSA can be expressed as

$$\begin{aligned} S_{sc}\left(f_a; r_0\right) = & W_a\left[\frac{f_a - q_2 t_p}{\left(-q_2 + s_{fdr} f_{dr0}\right) T_s}\right] \\ & \exp\left\{-j\pi \frac{t_p}{\alpha_a} f_a + \frac{j\pi}{-q_2 + s_{fdr} f_{dr0}} f_a^2 \right. \\ & \left. + \frac{j\pi\left(-q_3 + s_{fdr} p_3 f_{dr0}^3\right)}{\left(-q_2 + s_{fdr} f_{dr0}\right)^3} f_a^3 + \frac{j\pi\left(q_4 + p_4 f_{dr0}^4\right)}{\left(-q_2 + s_{fdr} f_{dr0}\right)^4} f_a^4 \right\} \end{aligned} \tag{31}$$

Equation (31) indicates that azimuth variances of Doppler parameters are eliminated after RANCSA, and uniform focusing operation can be performed to Equation (31). The matched filter can be written as

$$\begin{aligned} S_{ac}\left(f_a; r_0\right) = \exp & \left\{ -\frac{j\pi}{-q_2 + s_{fdr} f_{dr0}} f_a^2 - \frac{j\pi\left(-q_3 + s_{fdr} p_3 f_{dr0}^3\right)}{\left(-q_2 + s_{fdr} f_{dr0}\right)^3} f_a^3 \right. \\ & \left. - \frac{j\pi\left(q_4 + p_4 f_{dr0}^4\right)}{\left(-q_2 + s_{fdr} f_{dr0}\right)^4} f_a^4 \right\} \end{aligned} \tag{32}$$

After multiplying Equation (31) by Equation (32) and applying the azimuth inverse Fourier transformation, the image is obtained and can be expressed as

$$s\left(\tau, t; r_0, t_p\right) = \sin c\left(\tau - \frac{2r_0}{c}\right) \cdot \sin c\left(t - \frac{t_p}{2\alpha_a}\right). \tag{33}$$

We can find that the target is focused at position $(r_0,\, \frac{x_p}{2\alpha_a})$, which is offset from the correct position. The azimuth elongated distortion can be easily corrected through geometric correction.

3.5.2. Choice of the Scaling Factor

When transforming from range-Doppler domain to 2-D time domain, the high order phases are neglected supposing quadratic phase is far larger than the high order phases. Moreover, from Equation (31) we can know that a spectrum broadening is introduced by RANCSA, if an ill-suited α_a is used, azimuth spectrum aliasing would occur. Therefore, we have:

$$\begin{cases} \left|a_{rt}t_pB_a + p_3B_a + p_4B_a^2\right| \ll \left|\frac{s_{fdr}}{f_{dr}}\right| \\ 2\left|-s_{fdr}\left(2\,\alpha_a - 1\right)f_{dr0}t_p\right| < prf - B_a \end{cases}. \tag{34}$$

HTQ is defined to indicate the relationship between quadratic order phase and high order phase:

$$HTQ = \left|a_{rt}t_pB_a + p_3B_a + p_4B_a^2\right| \cdot \left|f_{dr}\right| \tag{35}$$

The spectrum broadening magnitude and HTQ are presented in Figure 6. In Figure 6(a), the blue crosses stand for the magnitude of spectrum broadening, and the red solid line stands for the difference between PRF and Doppler bandwidth. If α_a is too far away from 0.5, the azimuth spectrum will be aliasing. In Figure 6(b), the blue solid line stands for HTQ. It is clear that if α_a is too close to 0.5, the error of Fourier transformation becomes huge. Therefore, the value of α_a should be chosen carefully.

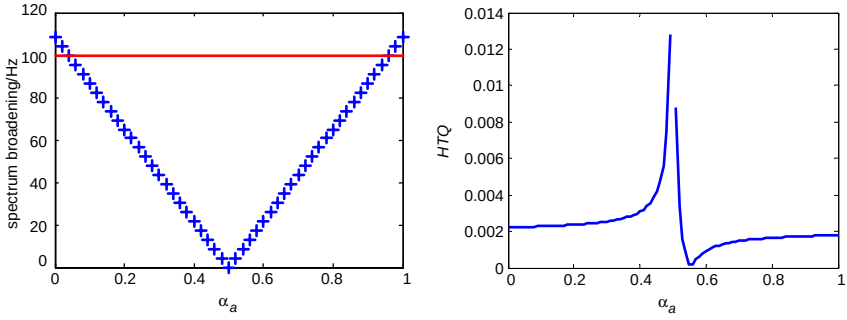

Figure 6. Spectrum broadening magnitude and HTQ with respect to α_a. (a) Spectrum broadening magnitude. (b) HTQ.

4. SIMULATION AND EXPERIMENTAL RESULTS

4.1. Verification of RSRM

In order to validate RSRM, two methods are adopted in this paper. First of all, the range errors of RSRM for modelling simulated slant

range histories are presented, and then the experiment results based on BeiDou navigation satellite operating on IGSO are proposed.

4.1.1. Range Errors Analysis of RSRM

The simulated slant range histories of GEO SAR at perigee, equator and apogee are illustrated in Figures 7(a)–(c) respectively, and then these slant range histories are modelled by RSRM and the range errors are proposed in Figure 7. The range errors at equator, apogee and perigee are of the order of 10^{-4} m, 10^{-6} m and 10^{-7} m respectively. They are far smaller than the resolution. Moreover, considering S-band SAR, the phase errors caused by the range error are less than $10^{-3}\pi$. Consequently, RSRM is accurate enough for GEO SAR imaging.

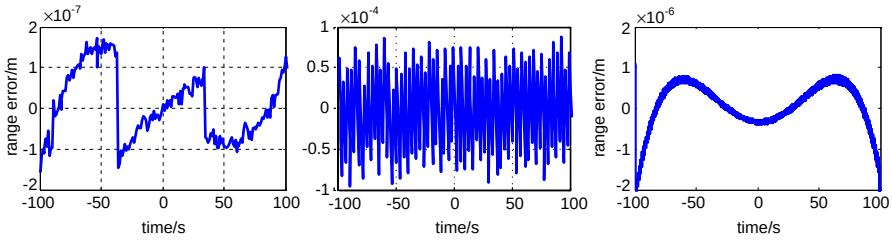

Figure 7. Range errors of RSRM in different position. (a) Perigee. (b) Equator. (c) Apogee.

4.1.2. Experiment Based on BeiDou Navigation Satellite

Because there is no GEO SAR satellite on orbit, it is difficult to validate RSRM by real echo data. Fortunately, there are five BeiDou navigation satellites operating on the same type of orbit as GEO SAR.

Therefore, a BeiDou navigation satellite is selected as the transmitter. A stationary antenna fixed on the top of a tall building is regarded as the receiver. The direct signal can be considered as the echo of a point target, and can be used to verify the correctness of RSRM. The system parameters of the selected satellite are listed in Table 1.

Figure 8 presents the experiment configuration and equipments. Figure 8(a) is the topology of the experiment. The signal source, receiver and data collector of the experiment are shown in Figure 8(b), and Figure 8(c) is the direct signal antenna. In this experiment, the synthetic aperture time is 600 seconds, and the position of satellite is close to apogee.

Table 1. System parameters of BeiDou.

Parameters	Values	Units
Carrier Frequency	1561.1	MHz
Code Type	CDMA	
Code Rate	2.046	M/s
Antenna Gain	13.5*	dB
Power	50*	W
Lowest Receiver Power	−158*	dBm
Orbit Altitude	35786	km
Best Range Resolution	15	m

∗: estimated values

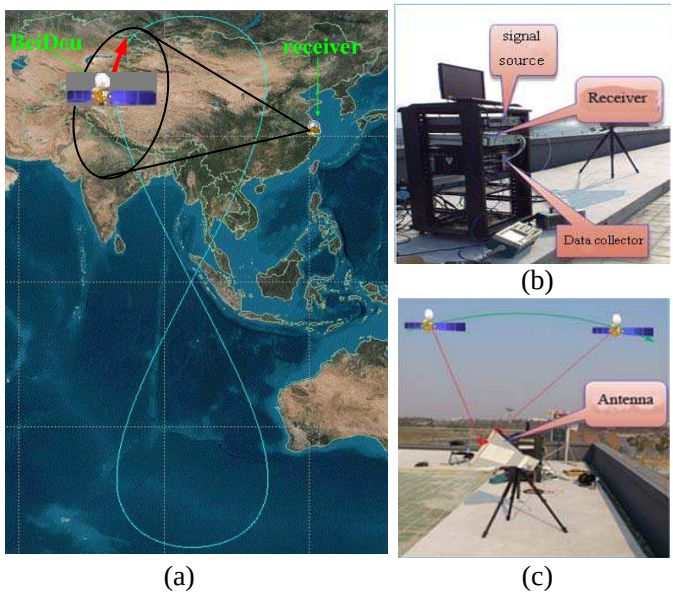

Figure 8. Experiment based on BeiDou. (a) Topology of the experiments. (b) The receiver, signal source and data collector of the experiment system. (c) Direct signal antenna.

The signal of BeiDou is pseudo-random code modulated navigation information and can be expressed as

$$s_{t\_c}(t) = A_e e(t) \exp(j2\pi f_c t + j\varphi + j\pi D_{e\_p}(t)) \tag{36}$$

where $e(t)$ is the transmitted code, A_e the amplitude of the transmitted

code, and $D_{e\_p}(t)$ the navigation information. Unlike the application of navigation, the navigation information must be removed in this experiment. Besides, the transmitted signal of navigation satellite are continuous, therefore the signal should be divided into the 2-D form firstly. Accordingly, the processing steps of the experiment are as follow [30]: firstly, time synchronization, frequency synchronization and navigation information removal are carried out; then, the signal is converted to the two-dimension form; finally, BPA based on SOA and RSRM are utilized to focus the experimental data respectively.

The range errors and images of different slant range models are given in Figure 9, and the images are projected on the ground plane. Obvious third order range error of SOA is found in Figure 9(a), and negligible range error of RSRM is shown in Figure 9(b). Correspondingly, as illustrated in Figure 9(c) and Figure 9(d), the image based on SOA suffers from severe resolution broadening and

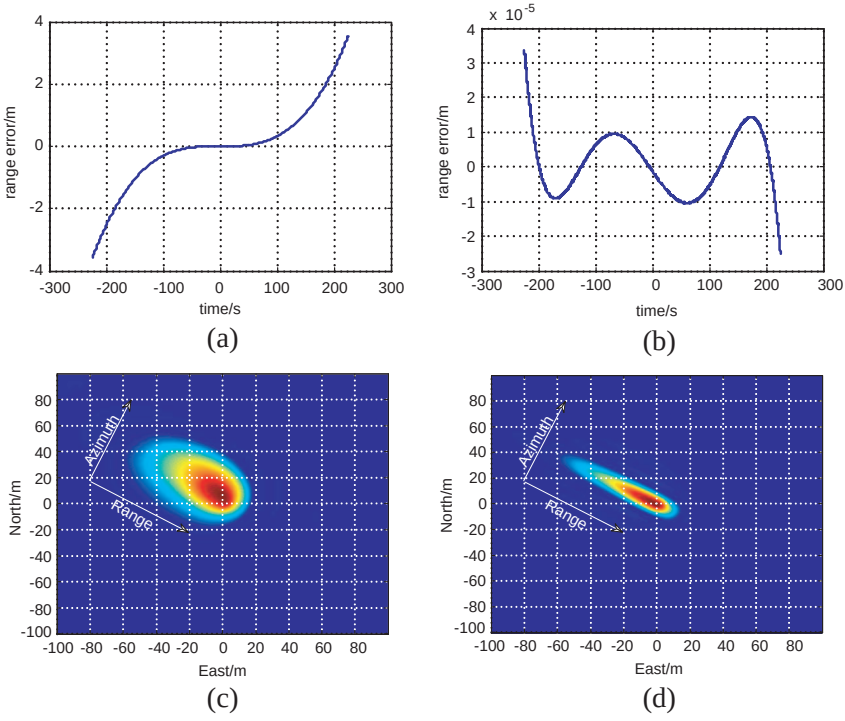

Figure 9. Experiment results based on BeiDou. (a) Range error of SOA. (b) Range error of RSRM. (c) Image based on SOA. (d) Image based on RSRM.

asymmetrical side lobes in azimuth direction, while that based on RSRM achieves good focusing. Consequently, the effectiveness of RSRM is validated through this experiment.

4.2. Analysis of 2-D Spectrum

In order to verify the precision of the 2-D spectrum, the echoes of point targets with different synthetic aperture times are compressed through spectra derived by approximate stationary points. The peak side lobe level ratios (PSLRs) with respect to synthetic aperture time are shown in Figure 10. The red $\times$ stands for theoretical limit of the PSLR, and the blue solid line denotes the measured values. The approximate stationary point can keep accurate even if the synthetic aperture time is up to 700 seconds. The synthetic aperture time of S-band GEO SAR is just about 200 seconds for resolution of 5 m. Therefore, the presented 2-D spectrum is accurate enough.

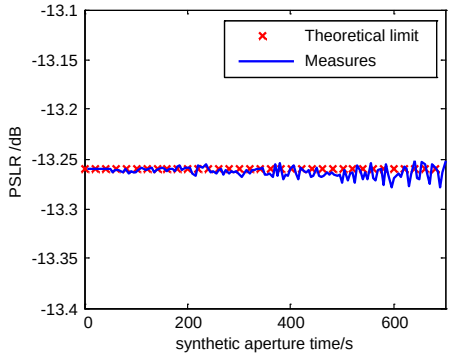

Figure 10. PSLR versus synthetic aperture time.

4.3. Imaging Algorithm Simulations

The presented RTNCSA is verified in this section. The simulation parameters are listed in Table 2, and the orbit elements are given in Section 2. So as to validate the RTNCSA for long synthetic aperture time and large scene focusing, a point array scene containing 121 point targets is constructed. The size of the scene is 150 km $\times$ 150 km and the targets are distributed in the whole scene uniformly, and the distance between point targets is 15 km in range and azimuth direction. The slant range images obtained by RTNCSA and NCSA in literature [20] at perigee and apogee are illustrated in Figure 11 and Figure 12

Table 2. Simulation parameters.

Parameters	Values	Units
Down-looking Angle	3.4	deg
Wavelength	0.09375	m
Bandwidth	60	MHz
Sampling Frequency	66.66	MHz
PRF	300	Hz
Imaging Scene	150	km
Synthetic aperture time	200	s

respectively. The evaluation results of 5 selected point targets are listed in Table 3 and Table 4.

In Figure 11 and Figure 12, the red solid lines stand for azimuth profiles of point targets obtained by RTNCSA and the blue dash-dot lines indicate that of NCSA. Clearly, as shown by the blue dash-dot lines, significant image degradation is introduced by resolution broadening, side lobe level increase and unsymmetrical side lobe toward the edges of the scene. As a comparison, the images obtained by RTNCSA are well focused.

Moreover, resolution, PSLR and integrated side lobe level ratio

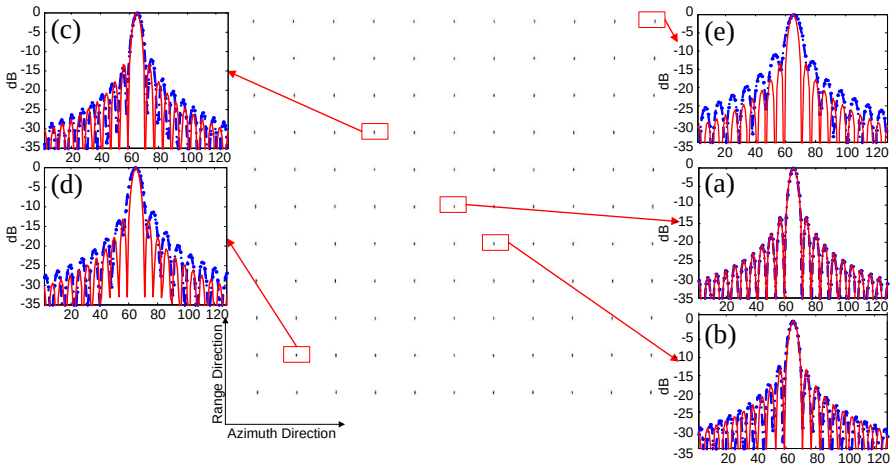

Figure 11. Images obtained by RTNCSA and NCSA at perigee. Red solid lines and blue dash-dot lines in (a)∼(e) stand for azimuth profiles of different point targets obtained by RTNCSA and NCSA respectively.

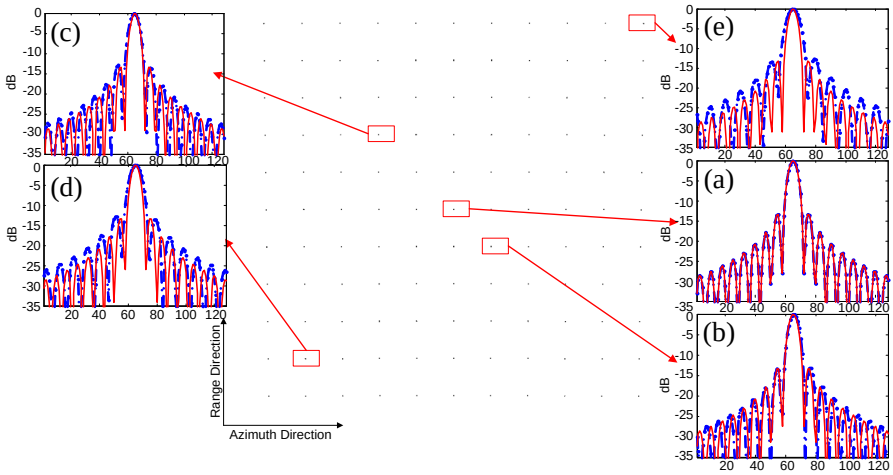

Figure 12. Images obtained by RTNCSA and NCSA at apogee. Red solid lines and blue dash-dot lines in (a)∼(e) stand for azimuth profiles of different point targets obtained by RTNCSA and NCSA respectively.

Table 3. Evaluation results of images obtained by RTNCSA and NCSA at perigee.

Position/ km	Resolution/m		PSLR/dB		ISLR/dB	
	Range	Azimuth	Range	Azimuth	Range	Azimuth
RTNCSA						
A (0, 0)	2.50	4.34	−13.39	−13.25	−10.21	−10.19
B (−15, 15)	2.50	4.32	−13.22	−13.23	−10.49	−10.84
C (30, −30)	2.49	4.35	−13.28	−13.21	−10.23	−10.37
D (−60, −60)	2.50	4.34	−13.32	−13.26	−10.30	−10.30
E (75, 75)	2.50	4.36	−13.27	−13.25	−10.05	−10.39
NCSA						
A (0, 0)	2.50	4.38	−13.31	−13.33	−10.20	−10.06
B (−15, 15)	2.50	4.42	−13.24	−11.84	−10.24	−9.93
C (30, −30)	2.50	4.51	−13.34	−10.68	−10.34	−9.51
D (−60, −60)	2.50	4.88	−13.31	−9.90	−10.23	−9.13
E (75, 75)	2.50	5.22	−13.25	−9.86	−10.18	−9.14

Table 4. Evaluation results of images obtained by RTNCSA and NCSA at apogee.

Position/ km	Resolution/m		PSLR/dB		ISLR/dB	
	Range	Azimuth	Range	Azimuth	Range	Azimuth
RTNCSA						
A (0, 0)	2.50	9.23	−13.32	−13.25	−10.15	−10.40
B (−15, 15)	2.50	9.24	−13.29	−13.23	−10.09	−10.50
C (30, −30)	2.50	9.31	−13.36	−13.22	−10.18	−10.83
D (−60, −60)	2.50	9.28	−13.26	−13.19	−10.28	−10.15
E (75,75)	2.50	9.27	−13.24	−13.22	−10.10	−10.15
NCSA						
A (0, 0)	2.50	9.26	−13.32	−13.29	−10.16	−10.14
B (−15, 15)	2.50	9.23	−13.10	−12.67	−10.01	−10.03
C (30, −30)	2.50	9.47	−13.13	−11.98	−10.09	−9.87
D (−60, −60)	2.50	9.48	−13.24	−10.11	−10.24	−8.47
E (75, 75)	2.50	10.00	−13.32	−8.63	−10.19	−7.91

(ISLR) are evaluated and listed in Table 3 and Table 4. As shown in Table 3 and Table 4, the slant range resolution is about 2.5 m at both perigee and apogee. The azimuth resolution at perigee is about 5 m. However, due to the slow relative satellite-Earth motion, the azimuth resolution at apogee is just about 10 m with the same synthetic aperture time. In addition, the images obtained by NCSA suffer from resolution broadening and side lobe level increase. And RTNCSA has better performances than NCSA in azimuth direction.

5. CONCLUSION

The RSRM and RTNCSA are proposed for GEO SAR in this paper. RSRM takes into account relative motion during long signal propagation time, curved orbit and "near-far-near" slant range histories at apogee. Although RSRM is precise enough for GEO SAR, the coefficients of RSRM vary dramatically both in range and azimuth direction. Therefore, RTNCSA based on RSRM is proposed to process echo with high resolution and large scene. Refined range nonlinear chirp scaling is adopted to correct space-variant RCM caused by range dependent effective velocities. And refined azimuth nonlinear chirp scaling is introduced to equalize the Doppler parameters in azimuth direction. Because there is no GEO SAR on orbit, a BeiDou navigation satellite operating on IGSO is selected to be transmitter,

and 600-second direct signal received by a stationary antenna on the top of a tall building is used to verify the effectiveness of RSRM. RTNCSA gives better performance than the NCSA for GEO SAR. And RTNCSA achieves almost theoretical performance for 150 km swath and synthetic aperture time up to 200 s of S-band. The RTNCSA in this paper is under an ideal acquisition. However, the impacts of many nonideal factors, such as depolarization and attenuation effects on the imaging algorithm are also very important, and will be our main work in the future.

APPENDIX A. PARAMETERS OF RSRM

Here, some expressions are given for some characteristics of the slant range model. The relative distance as a function of azimuth time can be approximated [31]

$$R(t) = \sqrt{\left|\vec{\mathbf{R}}(\mathbf{t})\right|^2} = r_0\left(1 + \frac{1}{2}x - \frac{1}{8}x^2 + \frac{1}{16}x^3 - \frac{5}{128}x^4\right) \tag{A1}$$

where $\vec{\mathbf{R}}(\mathbf{t})$ is the relative position vector of the satellite relative to the rotating Earth and

$$x = x_1 t + x_2 t^2 + x_3 t^3 + x_4 t^4 \tag{A2}$$

The x-coefficients can be expressed as

$$x_1 = \frac{2\vec{\mathbf{V}} \cdot \vec{\mathbf{R}}}{r_0^2} \tag{A3}$$

$$x_2 = \frac{\vec{\mathbf{R}} \cdot \vec{\mathbf{A}} + \vec{\mathbf{V}} \cdot \vec{\mathbf{V}}}{r_0^2} \tag{A4}$$

$$x_3 = \frac{\vec{\mathbf{A}} \cdot \vec{\mathbf{V}} + \frac{1}{3}\vec{\mathbf{R}} \cdot \vec{\mathbf{B}}}{r_0^2} \tag{A5}$$

$$x_4 = \frac{\frac{1}{3}\vec{\mathbf{V}} \cdot \vec{\mathbf{B}} + \frac{1}{12}\vec{\mathbf{R}} \cdot \vec{\mathbf{C}} + \frac{1}{4}\vec{\mathbf{A}} \cdot \vec{\mathbf{A}}}{r_0^2} \tag{A6}$$

where $\vec{\mathbf{V}}$, $\vec{\mathbf{A}}$, $\vec{\mathbf{B}}$ and $\vec{\mathbf{C}}$ are the relative velocity, acceleration, rate of acceleration, and the second derivate of the acceleration, respectively.

Then, the range cell migration is defined by

$$RCM = R(t) - r_0 = c_1 t + c_2 t^2 + c_3 t^3 + c_4 t^4 \tag{A7}$$

Therefore, the c-coefficients are given by

$$c_1 = \frac{r_0}{2} x_1 \tag{A8}$$

$$c_2 = \frac{r_0}{2}\left(x_2 - \frac{1}{4}x_1^2\right) \tag{A9}$$

$$c_3 = \frac{r_0}{2}\left(x_3 - \frac{x_1 x_2}{2} - \frac{1}{8}x_1^3\right) \tag{A10}$$

$$c_4 = \frac{r_0}{4}\left(2x_4 - x_1 x_3 - \frac{1}{2}x_2^2 + \frac{3}{4}x_1^2 x_2 - \frac{5}{32}x_1^4\right) \tag{A11}$$

The parameters of RURM in Equation (2) can be expressed as

$$v\left(r_0, x_0\right) = \sqrt{-2 s_{fdr} r_0 c_2} \tag{A12}$$

$$a\left(r_0, x_0\right) = c_3 \tag{A13}$$

$$b\left(r_0, x_0\right) = c_4 - \frac{s_{fdr} v^4}{8 r_0^3} \tag{A14}$$

APPENDIX B. COEFFICIENTS OF RANGE NCSA

Here, some coefficients of range nonlinear chirp scaling are presented. The difference between delay time from r_0 and that from reference range is

$$\tau\left(f_a; r_0\right) = \left(\frac{2\left(1 + s_{fdr}\right) r_0}{c} - \frac{2 s_{fdr} r_0}{c\gamma\left(r_0, f_a\right)}\right) - \left(\frac{2\left(1 + s_{fdr}\right) r_{ref}}{c} - \frac{2 s_{fdr} r_{ref}}{c\gamma\left(r_{ref}, f_a\right)}\right). \tag{B1}$$

Thus the slope of range-frequency rate is given by

$$K_s = \frac{s_{fdr} K_{mref}^2 \left(1 - \gamma^2\left(r_{ref}, f_a\right)\right)}{f_c \gamma^2\left(r_{ref}, f_a\right)} \left[1 - \frac{V_1 r_{ref}}{V_0 \gamma^2\left(r_{ref}, f_a\right) - 0.5 V_1 r_{ref}\left(1 - \gamma^2\left(r_{ref}, f_a\right)\right)}\right]. \tag{B2}$$

Besides, $\tau(f_a; r_0)$ can be expanded about r_{ref}, keeping terms up to the quadratic:

$$\tau\left(f_a; r_0\right) \approx a\left(f_a\right)\left(r_0 - r_{ref}\right) + b\left(f_a\right)\left(r_0 - r_{ref}\right)^2 \tag{B3}$$

where the coefficients in the expansion can be expressed as

$$a\left(f_a\right) = \frac{2\left(1 + s_{fdr}\right)}{c} - \frac{2 s_{fdr}}{c\gamma\left(r_{ref}, f_a\right)}\left[1 - \frac{r_{ref}\left(1 - \gamma^2\left(r_{ref}, f_a\right)\right)}{c\gamma^2\left(r_{ref}, f_a\right) V_0}\right] \tag{B4}$$

$$b\left(f_a\right) = \frac{s_{fdr}\left(1 - \gamma^2\left(r_{ref}, f_a\right)\right)}{c\gamma^3\left(r_{ref}, f_a\right)} \left(\frac{V_1}{V_0} + \frac{r_{ref} V_2}{V_0} - \frac{r_{ref} V_1^2}{V_0^2}\left(1 + \frac{3\left(1 - \gamma^2\left(r_{ref}, f_a\right)\right)}{4\gamma^2\left(r_{ref}, f_a\right)}\right)\right). \tag{B5}$$

Then the scaling factor in range chirp scaling phase function can be written as

$$\alpha_v(f_a) = \frac{a(f_a)}{a(f_{ar})} \tag{B6}$$

$$\beta_v(f_a) = \frac{1}{a^2(f_a)}\left[b(f_{ar}) - \frac{a(f_{ar})}{a(f_a)}b(f_a)\right]. \tag{B7}$$

ACKNOWLEDGMENT

This work was supported by the key project of National Natural Science Foundation of China (Grant Nos. 61001189, 61032009).

REFERENCES

1. Tomiyasu, K., "Synthetic aperture radar in geosynchronous orbit," *IEEE Antennas and Propagation Symp.*, Vol. 16, 42–45, University of Maryland, 1978.
2. Tomiyasu, K. and J. L. Pacelli, "Synthetic aperture radar imaging from an inclined geosynchronous orbit," *IEEE Trans. Geosci. Remote Sens.*, Vol. 21, No. 3, 324–329, 1983.
3. Chini, M., L. Pulvirenti, and N. Pierdicca, "Analysis and interpretation of the COSMO-SkyMed observations of the 2011 Japan Tsunami," *IEEE Geosci. Remote Sens. Lett.*, Vol. 9, No. 3, 467–471, 2012.
4. Zribi, M., F. Kotti, Z. Lili-Chabaane, et al., "Soil texture estimation over a semiarid area using TerraSAR-X radar data," *IEEE Geosci. Remote Sens. Lett.*, Vol. 9, No. 3, 353–357, 2012.
5. Wendy, E., M. Sore, M. Alina, and C. Curti, "Concepts and technologies for synthetic aperture radar from MEO and geosynchronous orbits," *SPIE International Asia-Pacific Symposium, Remote Sensing of the Atmosphere, Environment, and Space*, 195–203, USA, 2004.
6. Madsen, S. N., E. Wendy, L. D. DiDomenico, and L. John, "A geosynchronous synthetic aperture radar; for tectonic mapping, disaster management and measurements of vegetation and soil moisture," *2011 IEEE International Geoscience and Remote Sensing Symposium (IGARSS)*, Vol. 1, 447–449, 2001.
7. Evans, T. L. and M. Costa, "Landcover classification of the lower Nhecolandia subregion of the Brazilian pantanal wetlands using ALOS/PALSAR, RADARSAT-2 and ENVISAT/ASAR imagery," *Remote Sensing of Environment*, Vol. 128, 118–137, 2013.

8. NASA and JPL, "Global earthquake satellite system: A 20-year plan to enable earthquake prediction," JPL Document, 2003, http://solidearth.jpl.nasa.gov/GESS/3123GESSRep2003.pdf.
9. Hobbs, S. E. and D. Bruno, "Radar imaging from GEO: Challenges and applications," *Remote Sensing and Photogrammetry Society Annual Conference*, 1–6, 2007.
10. Bruno, D. and S. E. Hobbs, "Radar imaging from geosynchronous orbit: Temporal decorrelation aspects," *IEEE Transactions Geosci. Remote Sens.*, Vol. 48, No. 7, 2924–2929, 2010.
11. Hobbs, S. E., "GeoSAR summary of the group design project, MSc in Astronautics and Space Engineering 2005/06," 1–20, Cranfield University, 2006.
12. Mao, E. K., T. Long, T. Zeng, et al., "State-of-art of Geosynchronous SAR," *Signal Processing (Xinhao Chuli)*, Vol. 28, No. 4, 451–462, 2012.
13. Liu, F., C. Hu, and T. Zeng, "A novel range migration algorithm of GEO SAR echo data," *Proc. IGARSS*, 1–4, Jul. 2010.
14. Yang, W., Y. Zhu, F. Liu, C. Hu, and Z. Ding, "Modified range migration algorithm in GEO SAR system," *The 8th European Conference on Synthetic Aperture Radar*, 708–711, 2010.
15. Bao, M., Y. Liao, Z. J. Tian, et al., "Imaging algorithm for GEO SAR based on series reversion" *2011 IEEE CIE International Conference on Radar*, Vol. 2, 1493–1496, 2011.
16. Cheng, H., F. Liu, and W. Yang, "Modification of slant range model and imaging processing in GEO SAR," *Proc. IGARSS*, 4679–4682, Jul. 2010.
17. Hu, C., T. Zeng, Y. Zhu, and Z. Ding, "The accurate resolution analysis in Geosynchronous SAR," *The 8th European Conference on Synthetic Aperture Radar*, 925–928, 2010.
18. Bao, M., M. D. Xing, and Y. C. Li, "Chirp scaling algorithm for GEO SAR based on fourth-order range equation," *Electronics Letters*, Vol. 48, No. 1, 41–42, 2012.
19. Hu, C., Z. Liu, and T. Long, "An improved CS algorithm based on the curved trajectory in geosynchronous SAR," *IEEE Journal of Selected Topics in Applied Earth Observations and Remote Sensing*, Vol. 5, No. 3, 795–808, 2012.
20. Hu, C., T. Long, and Y. Tian, "An improved nonlinear chirp scaling algorithm based on curved trajectory in geosynchronous SAR," *Progress In Electromagnetics Research*, Vol. 135, 481–513, 2013.

21. Li, Z., C. Li, Z. Yu, et al., "Back projection algorithm for high resolution GEO-SAR image formation," *2011 IEEE International Geoscience and Remote Sensing Symposium (IGARSS)*, 336–339, 2011.
22. Tomiyasu, K., "Mitigation of rain and ice particle cross polarization at RF for dual circularly polarized waves," *IEEE Transactions on Antennas and Propagation*, Vol. 46, No. 9, 1379–1385, 1998.
23. Gao, Y. T., "The analysis and design of GEO SAR and the study of echo modeling," School of Information and Electronics, Beijing Institute of Technology, Beijing, 2011 (in Chinese).
24. Zeng, T., L. Liu, and Z. Ding, "Improved stepped-frequency SAR imaging algorithm with the range spectral-length extension Strategy," *IEEE Journal of Selected Topics in Applied Earth Observations and Remote Sensing*, Vol. 5, No. 5, 1483–1494, 2012.
25. Ding, Z, T. Long, T. Zeng, and Y. Zhu, "Deramp range migration processing for spaceborne spotlight synthetic aperture radar," *Advances in Space Research*, Vol. 41, No. 11, 1822–1826, 2008.
26. Davidson, G. W., I. G. Cumming, and M. R. Ito, "A chirp scaling approach for processing squint mode SAR data," *IEEE Trans. Aerosp. Electron. Syst.*, Vol. 32, No. 1, 121–133, 1996.
27. Wong, F. W. and T. S. Yeo, "New applications of nonlinear chirp scaling in SAR data processing," *IEEE Trans. Geosci. Remote Sens.*, Vol. 39, No. 5, 946–953, 2001.
28. Sun, G., X. Jiang, M. Xing, et al., "Focus improvement of highly squinted data based on azimuth nonlinear scaling," *IEEE Trans. Geosci. Remote Sens.*, Vol. 49, No. 6, 2308–2322, 2011.
29. An, D., X. Huang, T. Jin, et al., "Extended nonlinear chirp scaling algorithm for high-resolution highly squint SAR data focusing," *IEEE Trans. Geosci. Remote Sens.*, Vol. 50, No. 9, 3595–3609, 2012.
30. Liu, F., "Image formation and change detection based on space-surface BiSAR systems," School of Information and Electronics, Beijing Institute of Technology, Beijing, 2012 (in Chinese).
31. Eldhuset, K., "A new fourth-order processing algorithm for spaceborne SAR," *IEEE Trans. Aerosp. Electron. Syst.*, Vol. 34, No. 3, 824–835, 1998.